

UNIVERSIDAD DE CONCEPCIÓN



CENTRO DE INVESTIGACIÓN EN  
INGENIERÍA MATEMÁTICA (CI<sup>2</sup>MA)



Comparison of rigorous coupled-wave approach and finite  
element method for photovoltaic devices with periodically  
corrugated metallic backreflector

MUHAMMAD FARYAD, AKHLESH LAKHTAKIA,  
PETER MONK, MANUEL SOLANO

PREPRINT 2014-16

SERIE DE PRE-PUBLICACIONES



# Comparison of rigorous coupled-wave approach and finite element method for photovoltaic devices with periodically corrugated metallic backreflector

Manuel E. Solano,<sup>1</sup> Muhammad Faryad,<sup>2</sup> Akhlesh Lakhtakia,<sup>2</sup> and Peter B. Monk<sup>3,4</sup>

<sup>1</sup>*Departamento de Ingeniería Matemática – CPMA,  
Universidad de Concepción, Concepción, Chile*

<sup>2</sup>*Nanoengineered Metamaterials Group,  
Department of Engineering Science and Mechanics,  
Pennsylvania State University, University Park, PA 16802*

<sup>3</sup>*Department of Mathematical Sciences,  
University of Delaware, Newark, DE 19716*

<sup>4</sup>*Corresponding author: monk@math.udel.edu*

(Dated: June 20, 2014)

## Abstract

Optimal design of photovoltaic devices with a periodically corrugated metallic backreflector requires a rapid and reliable way to simulate the optical characteristics for wide ranges of wavelength and angle of incidence. Two independent numerical techniques are needed for confidence in numerical results. We compared the rigorous coupled-wave approach (RCWA) and the finite element method (FEM), the former being fast and flexible, but the latter having predictable convergence even for discontinuous constitutive properties. Depending on the shape of the corrugation and the constitutive properties of the metal and dielectric materials making up the device, both methods can exhibit slow convergence rates for  $p$ -polarized light. The chosen model problem in this paper is of this type. As rapid spatial variations of the fields are the underlying cause, suitable selective refinement of the FEM mesh can overcome this slow convergence. Therefore, it would be desirable to have a self-adaptive scheme for choosing the mesh in the FEM. This will slow down the algorithm, but will give a reliable way to check the RCWA results.

## I. INTRODUCTION

Optimal design of a photovoltaic (PV) solar cell requires the maximal entry of the insolation flux into the device followed by efficient absorption in the absorber layers. To achieve this goal using any optimization algorithm, the frequency-domain Maxwell equations must be repeatedly solved for wide ranges of optical frequencies and angles of incidence. The piecewise homogeneity of a PV device in the thickness direction does not offer serious roadblocks in design, because efficient methods for calculating the spatial profile of the electric field in a multilayered structure have been available for several decades [1–5]. However, nonhomogeneity that is wholly transverse to the thickness direction is far more complicated to handle, even when that nonhomogeneity is periodic.

Periodic nonhomogeneity of the metallic backreflector in a thin-film solar cell has attracted interest for over three decades, in order to enhance light trapping and enhance the generation of electron-hole pairs [6–12]. Optimization of the shape and the size of the unit cell of the metallic backreflector [13] is therefore very desirable. A similar configuration for planar optical concentrators may be optimized [14] in order to increase the cost-effectiveness of PV solar modules.

Solution of the frequency-domain Maxwell equations to optimize a PV device that is piecewise homogeneous in the thickness direction and has a periodically corrugated metallic backreflector can only be accomplished using numerical techniques, because applicable analytical techniques do not exist. The rigorous coupled-wave approach (RCWA) [15, 16], the finite element method (FEM) [17], the finite-difference time-domain (FDTD) method [18], and the method of moments [19] are well-known numerical techniques for this purpose. A coupling of evolutionary computation and genetic programming [20] with any one of these numerical techniques delivers an optimization tool for improving optical performance [13, 14]. However, as the underlying optical technique is purely numerical, the veracity of numerical results obtained by using it must be affirmed by comparison with results obtained using an independent numerical technique.

As we had earlier devised an optimization tool using the RCWA [13, 14], we decided to compare the RCWA and the FEM for a thin-film PV device that is piecewise homogeneous in the thickness direction and has a periodically corrugated metallic backreflector. In the RCWA, the relative permittivity everywhere is represented as a Fourier series, the

electromagnetic field phasors everywhere are represented in terms of Floquet harmonics in accordance with the Floquet–Bloch theorem, and a marching procedure is implemented [21, 22]. This method is fast. Also, it can readily accommodate changes in the shape of the unit cell and the spatial variation of the relative permittivity, since it does not require continuous space to be replaced by a mesh. However, the RCWA can be adversely affected by ill-conditioned matrices and the Gibbs phenomenon [21]. In contrast, the FEM is based on a mesh that must be generated afresh to adapt to changes in the unit cell. Moreover, special treatment is needed to handle the half spaces of incidence (and reflection) and transmission. Nevertheless, in general, the FEM has predictable convergence even for discontinuous constitutive properties [23].

In order to compare the RCWA and the FEM, we chose the representative boundary-value problem illustrated in Fig. 1. An isotropic dielectric multilayer backed by a periodically corrugated metallic backreflector is illuminated by an obliquely incident plane wave. Some or all of the layers may be absorber layers.

The plan of the paper is as follows: Theoretical preliminaries for both numerical techniques are presented in Sec. II, and numerical results are discussed in Sec. III. In Sec. IV we draw some conclusions. An  $\exp(-i\omega t)$  dependence on time  $t$  is implicit, with  $\omega$  denoting the angular frequency and  $i = \sqrt{-1}$ . The free-space wavenumber, the free-space wavelength, and the intrinsic impedance of free space are denoted by  $k_0 = \omega\sqrt{\epsilon_0\mu_0}$ ,  $\lambda_0 = 2\pi/k_0$ , and  $\eta_0 = \sqrt{\mu_0/\epsilon_0}$ , respectively, with  $\mu_0$  being the permeability and  $\epsilon_0$  the permittivity of free space. Vectors are in boldface, and the Cartesian unit vectors are identified as  $\hat{\mathbf{u}}_x$ ,  $\hat{\mathbf{u}}_y$ , and  $\hat{\mathbf{u}}_z$ .

## II. THEORETICAL PRELIMINARIES

### A. Boundary-value problem

The boundary-value problem is shown schematically in Fig. 1. In general, the relative permittivity  $\epsilon_r(x, z) = \epsilon_r(x \pm L, z)$  is a function of  $x \in (-\infty, \infty)$  with period  $L$ , and also varies with  $z \in (-\infty, \infty)$ . The half spaces  $z < 0$  and  $z > L_t = L_d + L_g + L_m$  are occupied by air; hence,  $\epsilon_r(x, z) \equiv 1$  in these regions. The region  $0 < z < L_d$  is occupied by the isotropic dielectric multilayer comprising  $N$  layers, numbered as shown in the figure. The thickness

and the relative permittivity of the  $j$ -th layer are denoted by  $d_j$  and  $\epsilon_{rj}$ ,  $j \in [1, N]$ , so that  $L_d = d_1 + d_2 + \dots + d_N$ . The region  $L_d + L_g < z < L_t$  is occupied by a spatially homogeneous metal with relative permittivity  $\epsilon_m$ .

The region  $L_d < z < L_d + L_g$  contains a periodically corrugated metal/dielectric interface of period  $L$  along the  $x$  axis. The relative permittivity  $\epsilon_r(x, z)$  in the reference unit cell  $0 < x < L$  of this region is given by

$$\epsilon_r(x, z) = \epsilon_{r1} + (\epsilon_m - \epsilon_{r1})\mathcal{U}[z - g(x)], \quad x \in (0, L), \quad z \in (L_d, L_d + L_g), \quad (1)$$

where

$$\mathcal{U}(\varphi) = \begin{cases} 1, & \varphi \geq 0 \\ 0, & \varphi < 0 \end{cases}, \quad (2)$$

is the unit step function. With  $\zeta \in [0, 1]$ , the function

$$g(x) = \begin{cases} L_d, & 2x/L \in (1 - \zeta, 1 + \zeta) \\ L_d + L_g, & 2x/L \in (0, 1 - \zeta) \cup (1 + \zeta, 2) \end{cases}, \quad (3)$$

describes the corrugation in the reference unit cell. Thus, the isotropic dielectric multilayer is backed by a rectangular metallic grating of period  $L$ , depth  $L_g$ , and duty cycle  $\zeta$ . The grating is filled by the same material as the first layer, and it rests on a metallic layer of thickness  $L_m$ .

The face  $z = 0$  of the described structure is illuminated by an obliquely incident plane wave whose electric field phasor is given by

$$\mathbf{E}_{inc}(\mathbf{r}) = [a_s \hat{\mathbf{u}}_y + a_p (-\hat{\mathbf{u}}_x \cos \theta + \hat{\mathbf{u}}_z \sin \theta)] \exp [ik_0 (x \sin \theta + z \cos \theta)], \quad z \leq 0. \quad (4)$$

Here,  $\theta$  is the angle of incidence with respect to the  $z$  axis,  $a_s$  is the amplitude of the  $s$ -polarized component, and  $a_p$  is the amplitude of the  $p$ -polarized component.

As depolarization cannot occur in this problem [11, 24], the electric field phasors of the reflected and the transmitted fields can be stated as

$$\mathbf{E}_{ref}(\mathbf{r}) = \sum_{n \in \mathbb{Z}} (a_s r_s^{(n)} \hat{\mathbf{u}}_y + a_p r_p^{(n)} \mathbf{p}_n^-) \exp [i (\kappa^{(n)} x - \alpha^{(n)} z)], \quad z < 0, \quad (5)$$

and

$$\mathbf{E}_{tr}(\mathbf{r}) = \sum_{n \in \mathbb{Z}} (a_s t_s^{(n)} \hat{\mathbf{u}}_y + a_p t_p^{(n)} \mathbf{p}_n^+) \exp (i [\kappa^{(n)} x + \alpha^{(n)} (z - L_t)]), \quad z > L_t, \quad (6)$$

respectively, where  $\mathbb{Z} \equiv \{0, \pm 1, \pm 2, \dots\}$ ,

$$\kappa^{(n)} = k_0 \sin \theta + 2\pi n/L, \quad (7)$$

$$\alpha^{(n)} = \begin{cases} +\sqrt{k_0^2 - (\kappa^{(n)})^2}, & k_0^2 \geq (\kappa^{(n)})^2 \\ +i\sqrt{(\kappa^{(n)})^2 - k_0^2}, & k_0^2 < (\kappa^{(n)})^2 \end{cases}, \quad (8)$$

and

$$\mathbf{p}_n^\pm = \mp \frac{\alpha^{(n)}}{k_0} \hat{\mathbf{u}}_x + \frac{\kappa^{(n)}}{k_0} \hat{\mathbf{u}}_z. \quad (9)$$

The index  $n = 0$  labels specular components, whereas nonspecular components are indicated by  $n \neq 0$ . The reflection coefficients of order  $n$  are denoted by  $r_s^{(n)}$  and  $r_p^{(n)}$ , and the corresponding transmission coefficients by  $t_s^{(n)}$  and  $t_p^{(n)}$ .

For an  $s$ -polarized incident plane wave, the absorptance is defined as

$$A_s = 1 - \sum_{n \in \mathbb{Z}} \left[ \left( |r_s^{(n)}|^2 + |t_s^{(n)}|^2 \right) \operatorname{Re}(\alpha^{(n)}) / \alpha^{(0)} \right], \quad (10)$$

and for a  $p$ -polarized incident plane wave it is given by

$$A_p = 1 - \sum_{n \in \mathbb{Z}} \left[ \left( |r_p^{(n)}|^2 + |t_p^{(n)}|^2 \right) \operatorname{Re}(\alpha^{(n)}) / \alpha^{(0)} \right]. \quad (11)$$

Both quantities are functions of  $\lambda_0$  and  $\theta$ . Often we want to maximize the polarization-averaged absorptance  $(A_s + A_p)/2$  of a PV device.

## B. Rigorous coupled-wave approach

The RCWA requires the expansion of the relative permittivity  $\epsilon_r$  in the region  $0 < z < L_t$  as a Fourier series with respect to  $x$ , viz.,

$$\epsilon_r(x, z) = \sum_{n \in \mathbb{Z}} \epsilon^{(n)}(z) \exp(i2\pi n x/L), \quad z \in (0, L_t). \quad (12)$$

For the problem depicted in Fig. 1,  $\epsilon^{(n)}(z)$  is a known piecewise constant function. The field phasors are written in the same region in terms of Floquet harmonics as

$$\left. \begin{aligned} \mathbf{E}(\mathbf{r}) &= \sum_{n \in \mathbb{Z}} [E_x^{(n)}(z) \hat{\mathbf{u}}_x + E_y^{(n)}(z) \hat{\mathbf{u}}_y + E_z^{(n)}(z) \hat{\mathbf{u}}_z] \exp(i\kappa^{(n)} x) \\ \mathbf{H}(\mathbf{r}) &= \sum_{n \in \mathbb{Z}} [H_x^{(n)}(z) \hat{\mathbf{u}}_x + H_y^{(n)}(z) \hat{\mathbf{u}}_y + H_z^{(n)}(z) \hat{\mathbf{u}}_z] \exp(i\kappa^{(n)} x) \end{aligned} \right\}, \quad z \in (0, L_t), \quad (13)$$

with unknown scalar functions  $E_{x,y,z}^{(n)}(z)$  and  $H_{x,y,z}^{(n)}(z)$ .

Expansions (12) and (13) are substituted in the frequency-domain Maxwell curl equations

$$\left. \begin{aligned} \nabla \times \mathbf{E} &= i\omega\mu_0\mathbf{H} \\ \nabla \times \mathbf{H} &= -i\omega\epsilon_0\epsilon_r(x, z)\mathbf{E} \end{aligned} \right\}, \quad z \in (0, L_t), \quad (14)$$

and the set  $\mathbb{Z}$  is replaced by the set  $\{0, \pm 1, \pm 2, \dots, \pm N_t\}$ , where  $N_t > 0$  is a finite integer. The result is a finite set of algebraic equations that are compactly describable in matrix notation [25, Sec. 2.3.4]. A numerically stable algorithm [15, 16, 22] can then be used to find the reflection coefficients  $\left\{r_s^{(n)}\right\}_{n=-N_t}^{N_t}$  and  $\left\{r_p^{(n)}\right\}_{n=-N_t}^{N_t}$  as well as the transmission coefficients  $\left\{t_s^{(n)}\right\}_{n=-N_t}^{N_t}$  and  $\left\{t_p^{(n)}\right\}_{n=-N_t}^{N_t}$ .

### C. Finite element method

After decoupling the  $s$ - and  $p$ -polarization states and noticing that the fields do not depend on  $y$ , Eqs. (14) reduce to the Helmholtz equation

$$\nabla \cdot [B(x, z)\nabla u(x, z)] + k_0^2\xi(x, z)u(x, z) = 0, \quad z \in (0, L_t), \quad (15)$$

where, depending on the polarization state,

$$u(x, z) = \begin{cases} E_y(x, z) \\ -\eta_0 H_y(x, z) \end{cases}, \quad B(x, z) = \begin{cases} 1 \\ 1/\epsilon_r(x, z) \end{cases}, \quad \xi(x, z) = \begin{cases} \epsilon_r(x, z) \\ 1 \end{cases}, \quad (16)$$

$$\text{polarization state} = \begin{cases} s \\ p \end{cases}. \quad (17)$$

Equations (4)–(6) lead to the expansions

$$u^-(x, z) = a_q \left\{ \exp[ik_0(x \sin \theta + z \cos \theta)] + \sum_{n \in \mathbb{Z}} r_q^{(n)} \exp[i(\kappa^{(n)}x - \alpha^{(n)}z)] \right\}, \quad z < 0, \quad (18)$$

and

$$u^+(x, z) = a_q \sum_{n \in \mathbb{Z}} t_q^{(n)} \exp\{i[\kappa^{(n)}x + \alpha^{(n)}(z - L_t)]\}, \quad z > L_t, \quad (19)$$

where  $q \in \{p, s\}$ .

The functions  $u$ ,  $u^+$  and  $u^-$  must be matched using suitable transmission conditions across the interfaces  $z = 0$  and  $z = L_t$ . In particular, depending on the polarization state,

either  $E_y$  or  $H_y$  must satisfy the standard electromagnetic boundary conditions at these interfaces; hence,

$$\left. \begin{aligned} \frac{\partial u^-}{\partial z} \Big|_{z=0} &= B(x, 0) \frac{\partial u}{\partial z} \Big|_{z=0} \\ \frac{\partial u^+}{\partial z} \Big|_{z=L_t} &= B(x, L_t) \frac{\partial u^+}{\partial z} \Big|_{z=L_t} \\ u^- \Big|_{z=0} &= u \Big|_{z=0} \\ u^+ \Big|_{z=L_t} &= u \Big|_{z=L_t} \end{aligned} \right\}, \quad x \in (0, L). \quad (20)$$

To accomplish this, we define two families of solutions as follows. The functions  $u_n^{(m)}(x, z)$ ,  $n \in \mathbb{Z}$  are solutions of the system of equations

$$\begin{aligned} \nabla \cdot [B(x, z) \nabla u_n^{(m)}(x, z)] + k_0^2 \xi(x, z) u_n^{(m)}(x, z) &= 0, \quad z \in (0, L_t), \quad x \in (0, L), \\ B(x, 0) \frac{\partial u_n^{(m)}}{\partial z} \Big|_{z=0} &= -\exp(i\kappa^{(n)} x), \quad x \in (0, L), \\ B(x, L_t) \frac{\partial u_n^{(m)}}{\partial z} \Big|_{z=L_t} &= 0, \quad x \in (0, L), \end{aligned} \quad (21)$$

subject to the quasiperiodicity conditions

$$\left. \begin{aligned} u_n^{(m)} \Big|_{x=L} &= \exp(ik_0 L \sin \theta) u_n^{(m)} \Big|_{x=0} \\ \frac{\partial u_n^{(m)}}{\partial x} \Big|_{x=L} &= \exp(ik_0 L \sin \theta) \frac{\partial u_n^{(m)}}{\partial x} \Big|_{x=0} \end{aligned} \right\}, \quad z \in (0, L_t). \quad (22)$$

Likewise, the functions  $u_n^{(p)}(x, z)$ ,  $n \in \mathbb{Z}$  are the solutions of the system of equations

$$\left. \begin{aligned} \nabla \cdot [B(x, z) \nabla u_n^{(p)}(x, z)] + k_0^2 \xi(x, z) u_n^{(p)}(x, z) &= 0, \quad z \in (0, L_t) \\ B(x, 0) \frac{\partial u_n^{(p)}}{\partial z} \Big|_{z=0} &= 0 \\ B(x, L_t) \frac{\partial u_n^{(p)}}{\partial z} \Big|_{z=L_t} &= \exp(i\kappa^{(n)} x), \end{aligned} \right\}, \quad x \in (0, L), \quad (23)$$

and also satisfy the quasiperiodicity conditions

$$\left. \begin{aligned} u_n^{(p)} \Big|_{x=L} &= \exp(ik_0 L \sin \theta) u_n^{(p)} \Big|_{x=0} \\ \frac{\partial u_n^{(p)}}{\partial x} \Big|_{x=L} &= \exp(ik_0 L \sin \theta) \frac{\partial u_n^{(p)}}{\partial x} \Big|_{x=0} \end{aligned} \right\}, \quad z \in (0, L_t). \quad (24)$$

Then, by virtue of the principle of superposition, the solution of Eq. (15) can be decomposed using these two sets of fields

$$u(x, z) = \sum_{n \in \mathbb{Z}} \gamma_n^{(m)} u_n^{(m)}(x, z) + \sum_{n \in \mathbb{Z}} \gamma_n^{(p)} u_n^{(p)}(x, z), \quad x \in (0, L), \quad z \in (0, L_t), \quad (25)$$

where the coefficients  $\gamma_n^{(m)}$  and  $\gamma_n^{(p)}$ ,  $n \in \mathbb{Z}$ , have to be determined.

To implement the method, the index set  $\mathbb{Z}$  in Eqs. (18), (19), and (25) is truncated to the set  $-M_t \leq n \leq M_t$  where  $M_t > 0$  is a finite integer. Equations (21)–(24) are approximated using the FEM in the rectangular region  $\{(x, z) \mid x \in (0, L), z \in (0, L_t)\}$ ; hence, this region is covered by a mesh of  $N_e$  triangular elements [17]. Every function on the right side of Eq. (25) is represented as a standard continuous piecewise cubic finite-element function satisfying the relevant quasiperiodicity conditions exactly. The FEM yields approximate values of the functions  $u_n^{(p)}(x, z)$  or  $u_n^{(m)}(x, z)$ ,  $-M_t \leq n \leq M_t$  at the interpolation points.

Use of the finite-element solutions in the truncated version of Eq. (25) followed by the use of the result in Eqs. (20) gives a system of algebraic equations for the expansion coefficients. For example, at  $z = L_t$  the approximate continuity of the normal derivative, per Eq. (20)<sub>2</sub>, requires that

$$i\alpha^{(n)} a_q t_q^{(n)} = -\gamma_n^{(p)}, \quad -M_t \leq n \leq M_t, \quad (26)$$

while the approximate continuity of the function values, per Eq. (20)<sub>4</sub>, requires that

$$L a_q t_q^{(n)} = \int_0^L \left( \sum_{n \in \mathbb{Z}} \gamma_n^{(m)} u_n^{(m)}(x, L_t) + \sum_{n \in \mathbb{Z}} \gamma_n^{(p)} u_n^{(p)}(x, L_t) \right) \exp(-i\kappa^{(n)} x) dx, \quad -M_t \leq n \leq M_t. \quad (27)$$

Similar equations hold at  $z = 0$ . Then we can solve these truncated equations and determine the coefficients  $\left\{ \gamma_n^{(p)}, \gamma_n^{(m)} \right\}_{n=-M_t}^{M_t}$ ,  $\left\{ r_s^{(n)} \right\}_{n=-M_t}^{M_t}$ ,  $\left\{ r_p^{(n)} \right\}_{n=-M_t}^{M_t}$ ,  $\left\{ t_s^{(n)} \right\}_{n=-M_t}^{M_t}$ , and  $\left\{ t_p^{(n)} \right\}_{n=-M_t}^{M_t}$ .

### III. NUMERICAL RESULTS AND DISCUSSION

If  $L \ll \lambda_0$ , the metallic backreflector appears to be quite flat and all nonspecular modes are evanescent as  $|z| \rightarrow \infty$ . If, however,  $L$  is only somewhat smaller than  $\lambda_0$ , then the coupling of the solar flux to the dielectric layers in the PV device is enhanced [10]. Since the solar flux at sea level is mostly confined to  $\lambda_0 \in [400, 1100]$  nm with the high magnitudes in

a 225-nm-broad plateau centered about  $\lambda_0 = 560$  nm, we fixed  $L = 400$  nm for all numerical results presented here. Furthermore, based on experience with RCWA [11, 13, 14, 24] that convergence with respect to  $N_t$  is harder to achieve at shorter wavelengths, we also fixed  $\lambda_0 = 450$  nm for all numerical results presented here.

The isotropic dielectric multilayer was taken to comprise  $N = 9$  layers of silicon oxynitrides of different compositions. While the layer thickness  $d_j = 100$  nm was fixed for all  $j \in [1, N]$ , the relative permittivities at  $\lambda_0 = 450$  nm are as follows [26]:  $\epsilon_{r1} = 3.6876$ ,  $\epsilon_{r2} = 3.1656$ ,  $\epsilon_{r3} = 3.0413$ ,  $\epsilon_{r4} = 2.9045$ ,  $\epsilon_{r5} = 2.7124$ ,  $\epsilon_{r6} = 2.5691$ ,  $\epsilon_{r7} = 2.4297$ ,  $\epsilon_{r8} = 2.32101$ , and  $\epsilon_{r9} = 2.1886$ . The metal was taken to be evaporated silver with a relative permittivity  $\epsilon_m = -5.8828 + i0.6650$  at  $\lambda_0 = 450$  nm [24]. We fixed the thickness  $L_m = 40$  nm to exceed the skin depth of silver, in order to ensure very small transmittance into the half space  $z > L_t$ . Furthermore, we fixed  $\zeta = 0.5$  and  $L_g \in \{0, 25\}$  nm [13].

Computational codes for both the RCWA and the FEM were written in Matlab<sup>®</sup> and implemented on the LINUX machine Dell PowerEdge R620 configured with 15K SAS Drives and 320 GB of RAM. Version 2013a of Matlab uses 64 bits to represent any number. When implementing the RCWA algorithm [22], the region  $0 < z < L_d$  was divided into nine equally thick slices, the region  $L_d < z < L_d + L_g$  into a single slice, and the region  $L_d + L_g < z < L_t$  into a single slice. Had the corrugations not been rectangular, the region  $L_d < z < L_d + L_g$  would have been divided into as many slices as needed to ensure the stability of the technique. The FEM was taken to comprise  $N_e$  triangular elements, the interpolation polynomials were chosen to be cubic, and the mesh was configured so that each element contained just one homogeneous material. The error associated with the replacement of  $\mathbb{Z}$  in Eqs. (20) and (25) by the set  $\{0, \pm 1, \pm 2, \dots, \pm M_t\}$  decays exponentially when  $M_t$  is chosen large enough [27]. After some trial runs, we set  $M_t = 20$  so that this truncation error is negligible compared to the error of solving Eqs. (21) and (25) by FEM for the chosen boundary-value problem.

### A. Planar backreflector

We began with the simple case of a planar back-reflector (i.e.,  $L_g = 0$ ) to test the basic convergence rate of the FEM algorithm, since the RCWA provides the exact solution for

this case. We computed the errors

$$\left. \begin{aligned} e_{Eq} &= \frac{1}{|a_q|} \left( \int_{x=0}^L \int_{z=0}^{L_t} |\mathbf{E}_q(x, z) - \mathbf{E}_q^{FEM}(x, y)|^2 dz dx \right)^{1/2} \\ e_{Aq} &= |A_q - A_q^{FEM}| \end{aligned} \right\}, \quad q \in \{p, s\}, \quad (28)$$

in the electric field and the absorptance. Here,  $\mathbf{E}_q(x, z)$  is the exact electric field phasor and  $\mathbf{E}_q^{FEM}(x, z)$  is its approximate value yielded by the FEM, when the incident plane wave is  $q$  polarized; correspondingly,  $A_q$  is the exact absorptance and  $A_q^{FEM}$  is its FEM approximation.

We used a special-purpose finite-element meshing function based on the TRIANGLE library [28] to compute a sequence of successively finer meshes indexed by the integer  $\ell$ . For both the electric field and the absorptance, the following rates of convergence were defined:

$$\left. \begin{aligned} r_{Eq}^{(\ell)} &= 2 \log \left[ e_{Eq}^{(\ell)} / e_{Eq}^{(\ell+1)} \right] / \log \left[ N_e^{(\ell+1)} / N_e^{(\ell)} \right] \\ r_{Aq}^{(\ell)} &= 2 \log \left[ e_q^{(\ell)} / e_p^{(\ell+1)} \right] / \log \left[ N_e^{(\ell+1)} / N_e^{(\ell)} \right] \end{aligned} \right\}, \quad q \in \{p, s\}. \quad (29)$$

Here,  $e_{Eq}^{(\ell)}$  and  $e_{Aq}^{(\ell)}$  are the respective values of  $e_{Eq}$  and  $e_{Aq}$  when  $N_e = N_e^{(\ell)}$ ,  $N_e^{(\ell+1)} > N_e^{(\ell)}$ , and the  $(\ell + 1)$ -th mesh follows the  $\ell$ -th mesh in the hierarchy of meshes.

When the metallic backreflector is planar, the theory of FEM shows that the errors  $e_{Ep}$  and  $e_{Es}$  should be proportional to  $(1/\sqrt{N_e})^3$  and  $(1/\sqrt{N_e})^4$ , respectively, provided that the mesh is regular and quasiuniform [23, 27]. This means that the respective theoretical rates of convergence must converge to  $r_{Ep}^{(\infty)} = 3$  and  $r_{Es}^{(\infty)} = 4$  as the meshes are refined.

Table I displays the errors and the rates of convergence computed with respect to the number of elements  $N_e$ , when  $\theta = 0^\circ$ . The errors decay when the number of elements increases, as expected. We observe that the rates of convergence for the electric field are in excellent agreement with the theory for sufficiently large  $N_e$ , for both linear polarization states. Moreover, the table shows that  $r_{Ap}^{(\ell)} \rightarrow 4$  and  $r_{As}^{(\ell)} \rightarrow 4$  as  $\ell$  increases.

Once all the dielectric materials and the metal have been chosen, the rates of convergence should not depend on the angle of incidence (although the errors may vary with the angle of incidence due to resonances). These assertions can be justified through the results of simulations presented in Sec. IIIB for  $\theta = 30^\circ$ . The angle of incidence does affect the truncation error of the series in Eq. (25); however, as explained earlier in Sec. III, this error is negligible compared to the FEM error.

## B. Periodically corrugated backreflector

Let us now move on to the more complicated case of a periodically corrugated backreflector (i.e.,  $L_g > 0$ ). As the exact solution is not available in this case, we defined relative errors in the following manner. Suppose that  $\Theta$  is a discretization parameter such that  $\Theta = N_t$  for the RCWA and  $\Theta = \sqrt{N_e}$  for the FEM. Then, for both RCWA and FEM as well as for both linear polarization states of the incident light, the relative errors are given by

$$\left. \begin{aligned} \tilde{e}_{Eq} &= \frac{\left( \int_{x=0}^L \int_{z=0}^{L_t} |\mathbf{E}_q^{(\Theta_1)}(x, z) - \mathbf{E}_q^{(\Theta_2)}(x, z)|^2 dz dx \right)^{1/2}}{\left( \int_{x=0}^L \int_{z=0}^{L_t} |\mathbf{E}_q^{(\Theta_2)}(x, z)|^2 dz dx \right)^{1/2}} \\ \tilde{e}_{Aq} &= \left| \frac{A_q^{(\Theta_1)}}{A_q^{(\Theta_2)}} - 1 \right| \end{aligned} \right\}, \quad q \in \{p, s\}, \quad (30)$$

where  $\Theta_1$  and  $\Theta_2 > \Theta_1$  are two consecutive values of the discretization parameter. The sequence of relative errors of the same type is expected to converge as  $\Theta$  increases. The actual rates of convergence  $\tilde{r}_{Eq}$  and  $\tilde{r}_{Aq}$  were obtained, respectively, as the slope of the least-squares linear fits of the  $\log \tilde{e}_{Eq}$ -versus- $\log \Theta$  and  $\log \tilde{e}_{Aq}$ -versus- $\log \Theta$  data.

Figure 2 displays the errors  $\tilde{e}_{Es}$  and  $\tilde{e}_{Ep}$  as functions of  $\Theta$  for both RCWA and FEM, when  $\theta = 0^\circ$ . Whereas  $\log \tilde{e}_{Es}$  is almost proportional to  $\log \Theta$ ,  $\log \tilde{e}_{Ep}$  has an undulatory character, thereby making a prediction of the field intensities unreliable. Using the least-squares linear fits shown in the figure, we found that  $\tilde{r}_{Es} = 3.36$  for the FEM sequence but  $\tilde{r}_{Es} = 2.15$  for the RCWA sequence; likewise,  $\tilde{r}_{Ep} = 0.18$  for the FEM sequence but  $\tilde{r}_{Ep} = 0.14$  for the RCWA sequence. Thus, the FEM sequence converges faster than the RCWA sequence for light of either linear polarization states. This difference in performance may be attributed to the sharp changes in  $\epsilon_r(x, z)$  in the region  $L_d < z < L_d + L_g$ , to which the FEM is better adapted than the RCWA.

For related problems, Elschner and Schmidt [29] studied those properties of the solution of Eq. (15) that govern the rate of convergence. Although their FEM algorithm differs in detail from ours, their theory is relevant to any FEM algorithm. After considering the rapid variation of the solution near the corners of dissimilar materials, they concluded that the error  $\tilde{e}_{Ep}$  should decay with a rate  $\tilde{r}_{Ep} = 0.06$ . So the extremely low value of  $\tilde{r}_{Ep}$  that we obtained for the FEM is in approximate agreement with their theory.

Similar conclusions can be drawn for the sequences of  $\tilde{e}_{As}$  and  $\tilde{e}_{Ap}$  presented in Fig. 3 for

$\theta = 0^\circ$ , but the rates of convergence are higher. Thus,  $\tilde{r}_{As} = 4.33$  (FEM) and 3.25 (RCWA), while  $\tilde{r}_{Ap} = 0.62$  (FEM) and 0.14 (RCWA).

To highlight the influence of the constitutive properties on the convergence rates of RCWA or FEM, suppose that the metal is replaced by a dielectric material with relative permittivity  $\epsilon_m = 0.0187$ . For the  $p$ -polarization state, an application of Elschner and Schmidt's theory [29] predicts the FEM convergence rate of  $\tilde{r}_{Ep} = 0.5$  when  $\theta = 0^\circ$ . This is due to an improvement in the regularity of the solution  $u$  and should also be reflected in better convergence for the RCWA. Computationally, we obtained  $\tilde{r}_{Ep} = 0.87$  (FEM) and 0.92 (RCWA). As predicted, the convergence rate for the FEM increases in this case, although the rate is actually faster than predicted. The convergence rate of the RCWA also increases. So the relative permittivities of the materials in the device do affect the convergence of the FEM and RCWA algorithms and, since these relative permittivities can be allowed to vary in an optimization problem, the accuracy of the computational scheme may be difficult to assess.

The foregoing results suggest that selective mesh refinement in the FEM would be useful for  $p$ -polarized incidence. In fact, we can manually refine the mesh near the corners of the corrugations, since the electromagnetic field becomes singular at those corners [30]. In Fig. 4 we show an initial mesh and the first two refined meshes out of a sequence of nine meshes, the last six being too fine to be visualized on the same scale as the first three in the sequence. The values of  $\tilde{r}_{Ep}$  and  $\tilde{r}_{Ap}$  obtained using the last eight meshes in the sequence are plotted in Fig. 5 versus  $\Theta$ . Least-squares linear fitting of the data yields  $\tilde{r}_{Ep} = 0.94$  and  $\tilde{r}_{Ap} = 2.26$ , both improved from their respective values of 0.18 (Fig. 2) and 0.62 (Fig. 3) for the sequence of uniformly refined meshes. Moreover, the decay in  $\tilde{e}_{Ep}$  versus  $\Theta$  is not as oscillatory in Fig. 5 as in 2 and hence the FEM predictions are more reliable. Finally, we obtain a more accurate approximation with fewer elements. For example,  $\tilde{e}_{Ep} = 0.038$  for the uniformly refined mesh with  $N_e = 69360$  triangular elements, but it is matched by  $\tilde{e}_{Ep} = 0.037$  for the selectively refined mesh (near the corners of the corrugation) with just  $N_e = 4850$  triangular elements.

While the manually refined FEM (MRFEM) described in the previous paragraph works on a case-by-case basis, for optimal design we need an adaptive refinement procedure employing feedback from an *a-posteriori* error estimator that indicates which elements need further refinement in order to improve the solution. An *a-posteriori* error estimator identifies, without knowledge of the correct solution, all those elements in which the error is larger

than a given tolerance. Thus, those elements will be automatically refined in an self-adaptive FEM (SAFEM). In our simulations exemplified by Figs. 4 and 5, the triangular elements near the corners of the corrugation in the reference unit cell are refined, since we had observed that the errors are large in those elements. However it could happen that the errors are large also in other elements away from the corrugation. As our refinement might not be optimal, we are continuing towards the development of SAFEM algorithms.

We also determined from the MRFEM simulations that the angle of incidence  $\theta$  does not have a significant effect on the rates of convergence. In Figs. 6 and 7, we show the sequences of errors  $\tilde{e}_{Eq}$  and  $\tilde{r}_{Aq}$ , respectively, for both the RCWA and the MRFEM, when  $\theta = 30^\circ$ . The rates of convergence are (i)  $\tilde{r}_{Ep} = 0.26$ ,  $\tilde{r}_{Es} = 2.78$ ,  $\tilde{r}_{Ap} = 0.75$ , and  $\tilde{r}_{As} = 3.30$  for the RCWA and (ii)  $\tilde{r}_{Ep} = 0.80$ ,  $\tilde{r}_{Es} = 3.84$ ,  $\tilde{r}_{Ap} = 1.12$ , and  $\tilde{r}_{As} = 4.81$  for the MRFEM. Clearly, conclusions similar to those for normal incidence can be drawn.

### C. Computational time

A comparison of computational times versus performance of the RCWA and the MRFEM is now in order. As in Sec. III B, the backreflector is periodically corrugated. Furthermore, all results are presented for only normal incidence, because the angle of incidence has no influence on the computational time. For both the RCWA and MRFEM, the  $L^2$ -norm of the electric field was computed as

$$\|\mathbf{E}_q\| = \left( \int_{x=0}^L \int_{z=0}^{L_t} |\mathbf{E}_q^{(\Theta)}(x, y)|^2 dz dx \right)^{1/2}, \quad q \in \{p, s\} \quad (31)$$

for increasing values of  $\Theta$ .

Figures 8 and 9 present data on  $\|\mathbf{E}_q\|$  and  $A_q$ , respectively, in relation to  $\Theta$ . The MRFEM calculations were made with both  $M_t = 1$  and  $M_t = 20$ . Both figures also show the computational time in seconds. We excluded pre-processing times to initialize all variables for both the RCWA and MRFEM, implement Eq. (12) for the RCWA, and generate the MRFEM mesh. Let us note that the time elapsed in constructing the MRFEM mesh is negligible compared to the time spent in solving the equations involved.

The degrees of approximation of the electric field and the absorptance in MRFEM are not significantly affected whether  $M_t = 1$  or  $M_t = 20$ . Therefore, the truncation error of the series in Eqs. (20) and (25) is indeed very small compared to the MRFEM error, as we

mentioned at the beginning of Sec. III. Of course, taking  $M_t = 1$  considerably reduces the computational time since only three terms are used to approximate each series.

Figures 8 and 9 show that the RCWA and MRFEM provide similar results for the electric field and the absorptance when the incident light is  $s$  polarized. The latter figure shows that the converged values of the absorptance  $A_p$  computed with the two techniques differ by less than 1%. However, in Fig. 8, the converged values of  $\|\mathbf{E}_p\|$  computed with the two techniques differ by about 15%. This discrepancy is not surprising because the singular electric fields at and in the neighborhoods of metallic corners are difficult to capture with numerical techniques [31, 32].

Let us now discuss the computational time taken by each technique. The RCWA algorithm requires a partition of the interval  $(0, L_t)$  along the thickness direction into multiple slices, the thickness of each slice being chosen to ensure the stability of the technique. The computation of the absorptances  $A_s$  and  $A_p$  via Eqs. (10) and (11) consumes a minuscule amount of time after the reflection and the transmission coefficients have been obtained. But thinner slices (about 1 nm thick) are needed to accurately map the spatial variations of the fields induced inside the PV device. That is why the computation of the absorptances with the RCWA is much faster than the computation of the fields, as can be seen in Figs. 8 and 9. On the other hand, the fields and the absorptances are computed with same mesh parameters in the MRFEM. Hence, the time to compute both is the same.

In Fig. 8 the computational time for the MRFEM with  $M_t = 1$  is comparable in magnitude to that for the RCWA. Thus, both techniques require similar amounts of time to map out the fields induced inside a PV device. For the  $s$  polarization state, the RCWA delivered  $\tilde{e}_{Es} = 1.14 \times 10^{-3}$  in 0.76 s with  $\Theta = 5$ , whereas the MRFEM yielded  $\tilde{e}_{Es} = 2.85 \times 10^{-4}$  in 0.66 s with  $\Theta = 19$ . These are acceptable levels of error ( $< 1\%$ ). But for the  $p$  polarization state, neither technique performed as well. Given the limitation imposed on the magnitude of  $\Theta$  by our computing system, the RCWA yielded  $\tilde{e}_{Ep} = 6.45 \times 10^{-2}$  in 45 s with  $\Theta = 65$ , whereas the MRFEM delivered  $\tilde{e}_{Ep} = 3.82 \times 10^{-2}$  in 8.61 s with  $\Theta = 53.7$ . One could say that the MRFEM turned out to be faster and more accurate than the RCWA in this case.

In Fig. 9 the computational time for the MRFEM with  $M_t = 1$  is larger by an order of magnitude to that for the RCWA. For the  $p$  polarization state, the RCWA delivered  $\tilde{e}_{Ap} = 8.05 \times 10^{-3}$  in 0.62 s with  $\Theta = 65$ , whereas the MRFEM yielded  $\tilde{e}_{Ap} = 6.58 \times 10^{-3}$  in 0.76 s with  $\Theta = 26.4$ . Thus, the RCWA is about 18% faster. But for the  $s$  polarization

state, the RCWA is faster by almost two orders of magnitude:  $\tilde{e}_{As} = 7.06 \times 10^{-4}$  in 0.01 s with  $\Theta = 5$  whereas, in contrast, the MRFEM provided  $\tilde{e}_{As} = 2.00 \times 10^{-4}$  in 0.67 s with  $\Theta = 19$ .

#### IV. CONCLUSION

With the aim of determining the veracity of the results provided by numerical techniques to simulate the optical characteristic of photovoltaic devices with periodically corrugated metallic backreflector, we compared the performances of the rigorous coupled-wave approach and the finite element method. Whereas the RCWA is fast and flexible, the FEM has predictable convergence even for discontinuous constitutive properties. We found that the rates of convergence of the RCWA and FEM can be quite different for  $p$ -polarized light, but are generally the same for  $s$ -polarized light.

Due to the rapid spatial variations of electromagnetic fields in regions containing metallic edges and corners, both the RCWA and the FEM are slowly convergent for the  $p$  polarization state. Therefore, care needs to be exercised when using any numerical technique for this polarization state, and in particular a uniform mesh will not deliver a robust result. The mesh needs to be refined near the corners of the corrugation in the reference unit cell, ideally using a self-adaptive strategy.

Both the RCWA and the MRFEM deliver very similar values of the absorptances. The RCWA is somewhat faster than the MRFEM for the  $p$ -polarization state, and much faster for the  $s$ -polarization state. For the computation of the fields induced inside the PV device, the MRFEM is faster and more accurate than the RCWA. We hope that our investigations will assist in formulating robust and reliable procedures for the design of optimal PV devices.

*Acknowledgments.* MES acknowledges partial financial support from (i) CONICYT–Chile through grant FONDECYT-11130350, BASAL project CMM, Universidad de Chile and (ii) Centro de Investigación en Ingeniería Matemática (CI<sup>2</sup>MA), Universidad de Concepción. MF, AL, and PBM acknowledge partial financial support from US National Science Foun-

dation via grant DMR-1125590.

---

- [1] F. Abelès, “Recherches sur la propagation des ondes électromagnétiques sinusodales dans les milieux stratifiés. Application aux couches minces (1re partie),” *Ann. Phys. (Paris)* **5**, 596–640 (1950).
- [2] A. F. Huxley, “A theoretical treatment of the reflexion of light by multilayer structures,” *J. Exp. Biol.* **48**, 227–245 (1968).
- [3] S. Teitler and B. W. Hennis, “Refraction in stratified, anisotropic media,” *J. Opt. Soc. Am.* **60**, 830–834 (1970).
- [4] D. W. Berreman, “Optics in stratified and anisotropic media: 4×4-matrix formulation,” *J. Opt. Soc. Am.* **62**, 1502–510 (1972).
- [5] M. Born and E. Wolf, *Principles of Optics, 6th ed.* (Cambridge University Press, 1980); Sec. 1.6.
- [6] L. M. Anderson, “Parallel-processing with surface plasmons: a new strategy for converting the broad solar spectrum,” *Proc. 16th IEEE Photovoltaic Specialist Conf., San Diego, CA, Vol. 1*, pp. 371–377 (1982).
- [7] L. M. Anderson, “Harnessing surface plasmons for solar energy conversion,” *Proc. SPIE* **408**, 172–178 (1983).
- [8] P. Sheng, A. N. Bloch, and R. S. Stepleman, “Wavelength-selective absorption enhancement in thin-film solar cells,” *Appl. Phys. Lett.* **43**, 579–581 (1983).
- [9] C. Heine and R. H. Morf, “Submicrometer gratings for solar energy applications,” *Appl. Opt.* **34**, 2476–2482 (1995).
- [10] S. Mokkalapati and K. R. Catchpole, “Nanophotonic light trapping in solar cells,” *J. Appl. Phys.* **112**, 101101 (2012).
- [11] M. Faryad and A. Lakhtakia, “Enhancement of light absorption efficiency of amorphous-silicon thin-film tandem solar cell due to multiple surface-plasmon-polariton waves in the near-infrared spectral regime,” *Opt. Eng.* **52**, 087106 (2013).
- [12] M. Wellenzohn and R. Hainberger, “Insights in the light trapping effect in silicon solar cells with backside diffraction gratings,” *J. Photon. Energy* **3**, 034595 (2013).
- [13] M. Solano, M. Faryad, A. S. Hall, T. E. Mallouk, P. B. Monk, and A. Lakhtakia, “Optimization

- of the absorption efficiency of an amorphous-silicon thin-film tandem solar cell backed by a metallic surface-relief grating,” *Appl. Opt.* **52**, 966–979 (2013).
- [14] M. E. Solano, M. Faryad, P. B. Monk, T. E. Mallouk, and A. Lakhtakia, “Periodically multilayered planar optical concentrator for photovoltaic solar cells,” *Appl. Phys. Lett.* **103**, 191115 (2013).
- [15] N. Chateau and J.-P. Hugonin, “Algorithm for the rigorous coupled-wave analysis of grating diffraction,” *J. Opt. Soc. Am. A* **11**, 1321–1331 (1994).
- [16] M. G. Moharam, E. B. Grann, and D. A. Pommet, “Formulation for stable and efficient implementation of the rigorous coupled-wave analysis of binary gratings,” *J. Opt. Soc. Am. A* **12**, 1068–1076 (1995).
- [17] P. B. Monk, *Finite Element Methods for Maxwell’s Equations* (Oxford University Press, 2003).
- [18] A. Taflove and S. C. Hagness, *Computational Electrodynamics: The Finite-Difference Time-Domain Method, 3rd ed.* (Artech House, 2005).
- [19] T. Oğuzer and F. Kuyucuoğlu, “Method of moments solution by using sinc-type basis functions for the scattering from a finite number of conducting strip gratings,” *Turk. J. Elec. Eng.* **16**, 95–109 (2008)
- [20] W. Banzhaf, “Evolutionary computation and genetic programming,” Chap. 17 in: A. Lakhtakia and R. J. Martín-Palma, Eds., *Engineered Biomimicry* (Elsevier, 2013).
- [21] L. Li, “Use of Fourier series in the analysis of discontinuous periodic structures,” *J. Opt. Soc. Am. A* **13**, 1870–1876 (1996).
- [22] M. Faryad and A. Lakhtakia, “Grating-coupled excitation of multiple surface plasmon-polariton waves,” *Phys. Rev. A* **84**, 033852 (2011).
- [23] S. C. Brenner and L. R. Scott, *The Mathematical Theory of Finite Element Methods, 2nd ed.* (Springer, 2002).
- [24] M. Faryad, A. S. Hall, G. D. Barber, T. E. Mallouk, and A. Lakhtakia, “Excitation of multiple surface-plasmon-polariton waves guided by the periodically corrugated interface of a metal and a periodic multilayered isotropic dielectric material,” *J. Opt. Soc. Am. B* **29**, 704–713 (2012).
- [25] J. A. Polo, Jr., T. G. Mackay, and A. Lakhtakia, *Electromagnetic Surface Waves: A Modern Perspective* (Elsevier, 2013).
- [26] A. S. Hall, M. Faryad, G. D. Barber, L. Liu, S. Erten, T. S. Mayer, A. Lakhtakia, and T. E. Mallouk, “Broadband light absorption with multiple surface plasmon polariton waves excited

- at the interface of a metallic grating and photonic crystal,” ACS Nano **7**, 4995–5007 (2013).
- [27] N. H. Lord and A. J. Mulholland, “Explicit error bounds for the  $\alpha$ -quasi-periodic Helmholtz problem,” J. Opt. Soc. Am. A **30**, 2111–2123 (2013).
- [28] <http://www.cs.cmu.edu/~quake/triangle.html> (accessed 15 May 2014).
- [29] J. Elschner and G. Schmidt, “Diffraction in periodic structures and optimal design of binary gratings. Part I: direct problems and gradient formulas,” Math. Meth. Appl. Sci. **21**, 1297–1342 (1998).
- [30] M. Costabel and M. Dauge, “Singularities of electromagnetic fields in polyhedral domains,” Arch. Rational Mech. Anal. **151**, 221–276 (2000).
- [31] R. De Smedt, “Singular field behavior near the tip of a dielectric or dielectric-metallic corner,” Radio Sci. **22**, 1190–1996 (1987).
- [32] F. Assous, P. Ciarlet Jr., and E. Garcia, “A characterization of singular electromagnetic fields by an inductive approach,” Int. J. Num. Anal. Model. **5**, 491–515 (2008).

## List of Tables

**Table 1.** Errors and rates of convergence for the FEM when the metallic backreflector is planar and  $\theta = 0^\circ$ .

## List of Figures

**Fig. 1.** Schematic of the boundary-value problem solved using the RCWA and FEM. The specular and the non-specular components of the reflected and the transmitted fields are indicated on the diagram.

**Fig. 2.** Sequences of (top)  $\tilde{e}_{Es}$  and (bottom)  $\tilde{e}_{Ep}$  versus  $\Theta$  calculated with the RCWA (data points identified by +) and FEM (data points identified by  $\circ$ ) when  $\theta = 0^\circ$ . Errors cannot be defined for the initial value of  $\Theta$ . The dashed lines guide the reader's eyes. The solid lines are least-squares linear fits.

**Fig. 3.** Same as Fig. 2, except that (top)  $\tilde{e}_{As}$  and (bottom)  $\tilde{e}_{Ap}$  are displayed versus  $\Theta$ .

**Fig. 4.** (a) The initial FEM mesh and (b,c) the first two selectively refined meshes out of a sequence of nine meshes, the last six being too fine to be visualized on the same scale as the first three in the sequence. Increasing refinement occurs at the two corners of the corrugation in the reference unit cell.

**Fig. 5.** Sequences of  $\tilde{e}_{Ep}$  (data points identified by +) and  $\tilde{e}_{Ap}$  (data points identified by  $\circ$ ) versus  $\Theta$  calculated with the MRFEM when  $\theta = 0^\circ$ , for a sequence of nine meshes wherein the last eight are increasingly refined near the two corners of the corrugation in the reference unit cell. Errors cannot be defined for the initial mesh. The dashed lines guide the reader's eyes. The solid lines are least-squares line fits.

**Fig. 6.** Sequences of (top)  $\tilde{e}_{Es}$  and (bottom)  $\tilde{e}_{Ep}$  versus  $\Theta$  calculated with the RCWA (data points identified by +) and MRFEM (data points identified by  $\circ$ ) when  $\theta = 30^\circ$ . The dashed lines guide the reader's eyes. The solid lines are least-squares linear fits.

**Fig. 7.** Same as Fig. 6, except that (top)  $\tilde{e}_{As}$  and (bottom)  $\tilde{e}_{Ap}$  are displayed.

**Fig. 8.** Sequences of (top)  $\|\mathbf{E}_s\|$  and (bottom)  $\|\mathbf{E}_p\|$  versus  $\Theta$  calculated with the RCWA (data points identified by +), the MRFEM with  $M_t = 1$  (data points identified by  $\circ$ ), and the MRFEM with  $M_t = 20$  (datapoints identified by \*), when  $\theta = 0^\circ$ . The numbers stated near the data points are the computational times in seconds. The dashed lines guide the reader's eyes.

**Fig. 9.** Same as Fig. 8, except that (top)  $A_s$  and (bottom)  $A_p$  are displayed.

TABLE I. Errors and rates of convergence for the FEM when the metallic backreflector is planar and  $\theta = 0^\circ$ .

$\ell$	$N_e$	$e_{Ep}$	$r_{Ep}$	$e_{Es}$	$r_{Es}$	$e_{Ap}$	$r_{Ap}$	$e_{As}$	$r_{As}$
1	342	$3.46 \times 10^{-2}$	—	$5.72 \times 10^{-3}$	—	$9.70 \times 10^{-6}$	—	$4.30 \times 10^{-5}$	—
2	1880	$1.63 \times 10^{-3}$	3.58	$8.57 \times 10^{-5}$	4.93	$3.64 \times 10^{-6}$	1.15	$2.99 \times 10^{-6}$	3.13
3	7520	$2.05 \times 10^{-4}$	2.99	$5.29 \times 10^{-6}$	4.02	$1.97 \times 10^{-7}$	4.21	$1.91 \times 10^{-7}$	3.97
4	30080	$2.57 \times 10^{-5}$	3.00	$3.30 \times 10^{-7}$	4.01	$1.16 \times 10^{-8}$	4.08	$1.21 \times 10^{-8}$	3.98
5	120320	$3.22 \times 10^{-6}$	3.00	$2.06 \times 10^{-8}$	4.00	$7.07 \times 10^{-10}$	4.04	$7.58 \times 10^{-10}$	3.99

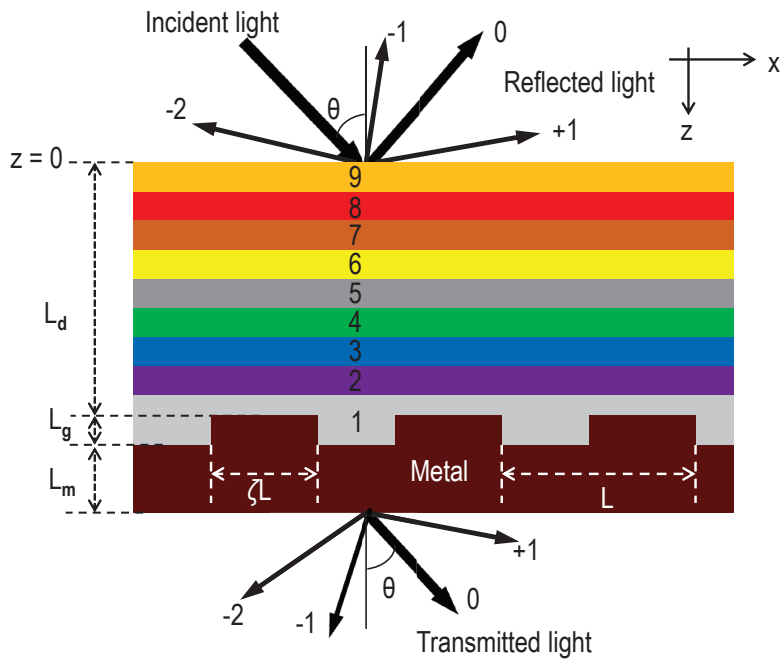


FIG. 1. Schematic of the boundary-value problem solved using the RCWA and the FEM. The specular and the non-specular components of the reflected and the transmitted fields are indicated on the diagram.

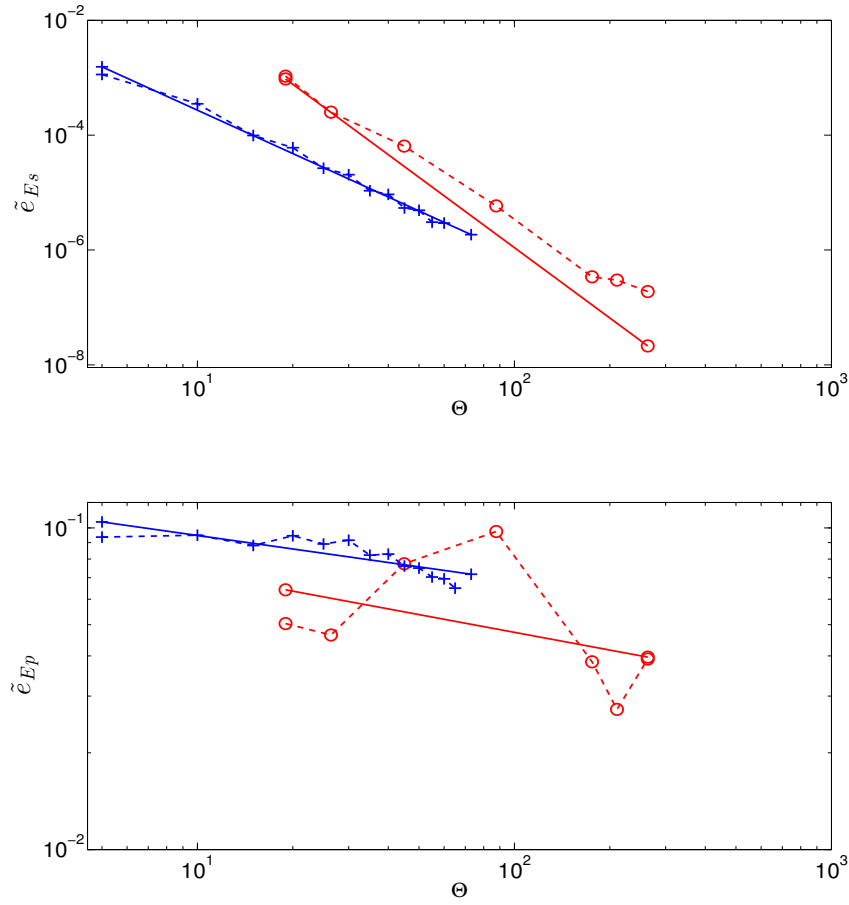


FIG. 2. Sequences of (top)  $\tilde{e}_{E_s}$  and (bottom)  $\tilde{e}_{E_p}$  versus  $\Theta$  calculated with the RCWA (data points identified by +) and FEM (data points identified by  $\circ$ ) when  $\theta = 0^\circ$ . Errors cannot be defined for the initial value of  $\Theta$ . The dashed lines guide the reader's eyes. The solid lines are least-squares linear fits.

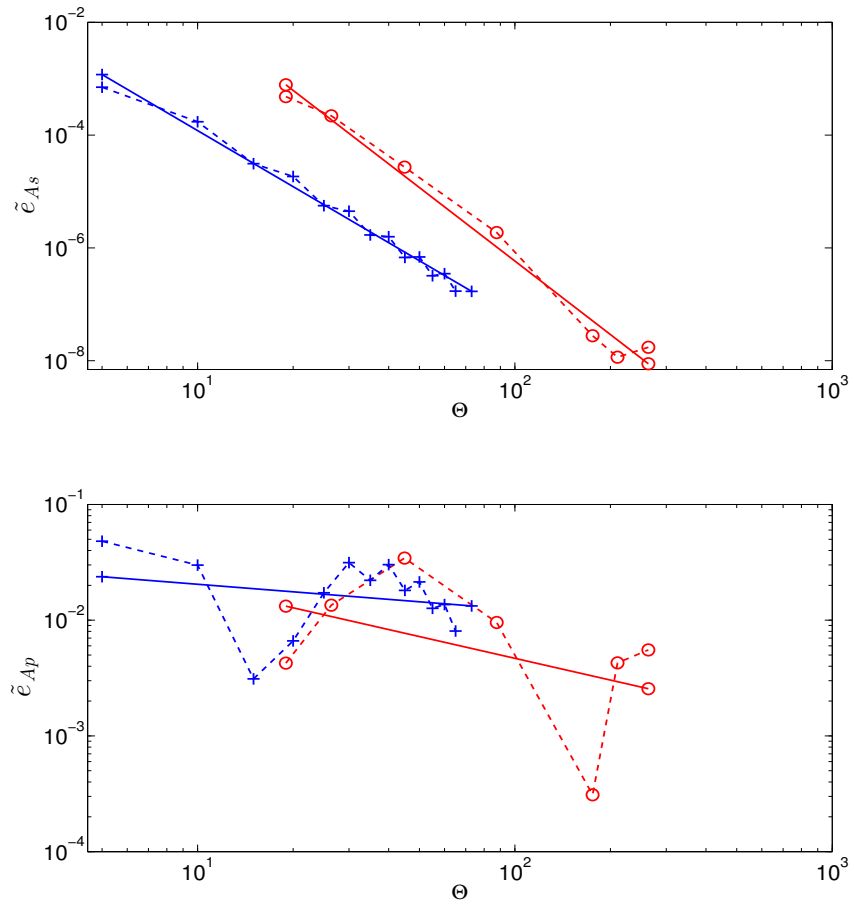


FIG. 3. Same as Fig. 2, except that (top)  $\tilde{e}_{As}$  and (bottom)  $\tilde{e}_{Ap}$  are displayed versus  $\Theta$ .

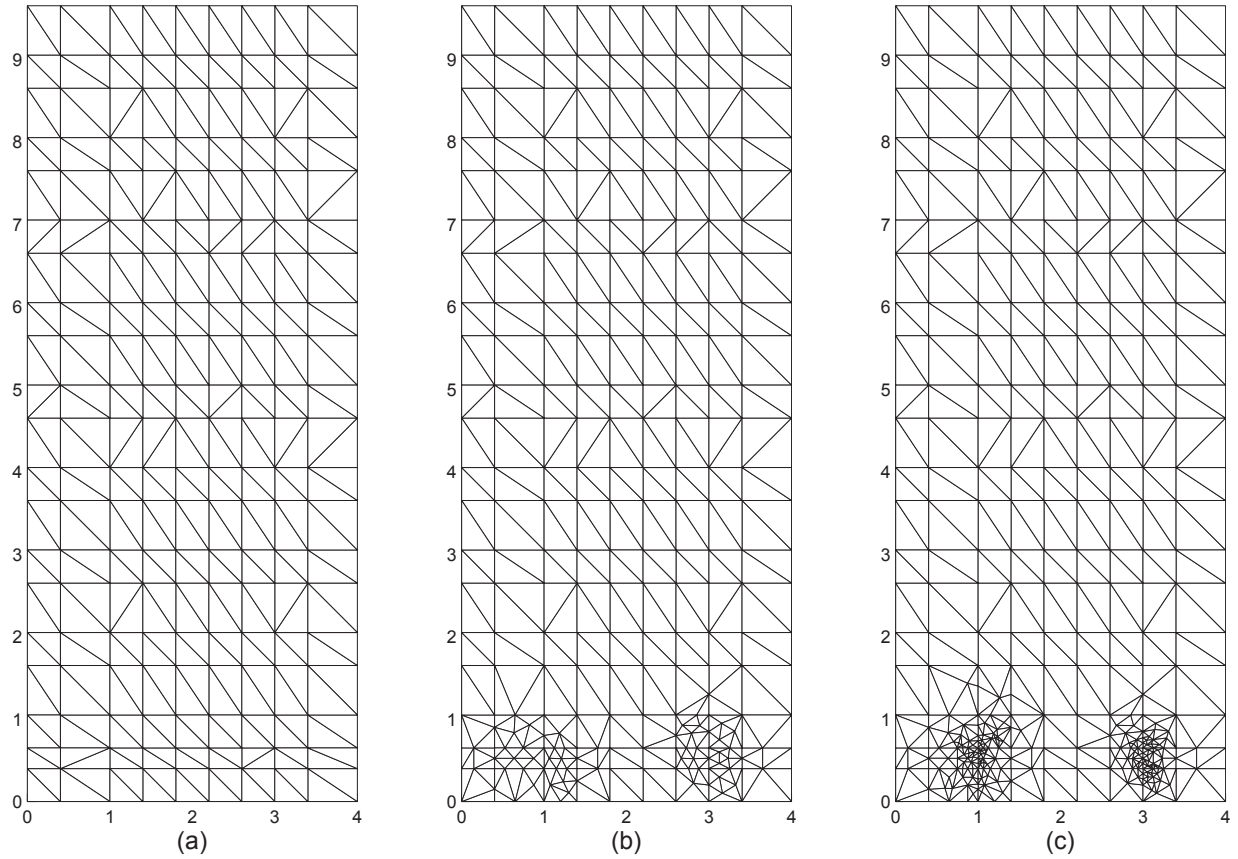


FIG. 4. (a) The initial FEM mesh and (b,c) the first two selectively refined meshes out of a sequence of nine meshes, the last six being too fine to be visualized on the same scale as the first three in the sequence. Increasing refinement occurs at the two corners of the corrugation in the reference unit cell.

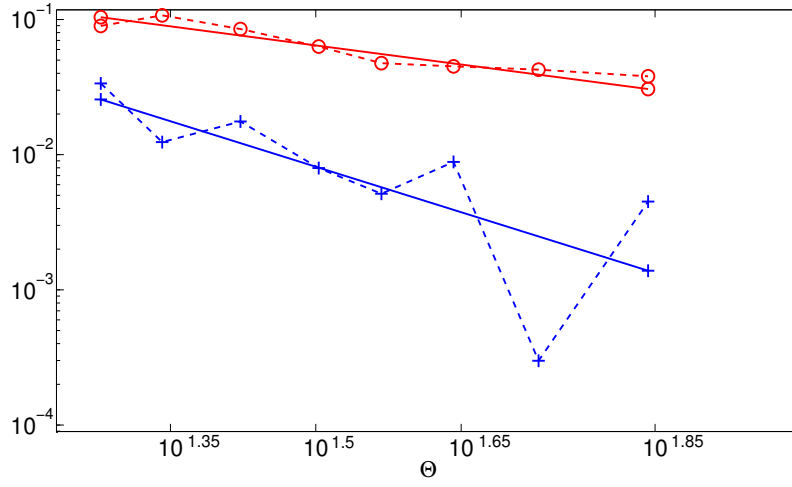


FIG. 5. Sequences of  $\tilde{e}_{Ep}$  (data points identified by +) and  $\tilde{e}_{Ap}$  (data points identified by o) versus  $\Theta$  calculated with the MRFEM when  $\theta = 0^\circ$ , for a sequence of nine meshes wherein the last eight are increasingly refined near the two corners of the corrugation in the reference unit cell. Errors cannot be defined for the initial mesh. The dashed lines guide the reader's eyes. The solid lines are least-squares line fits.

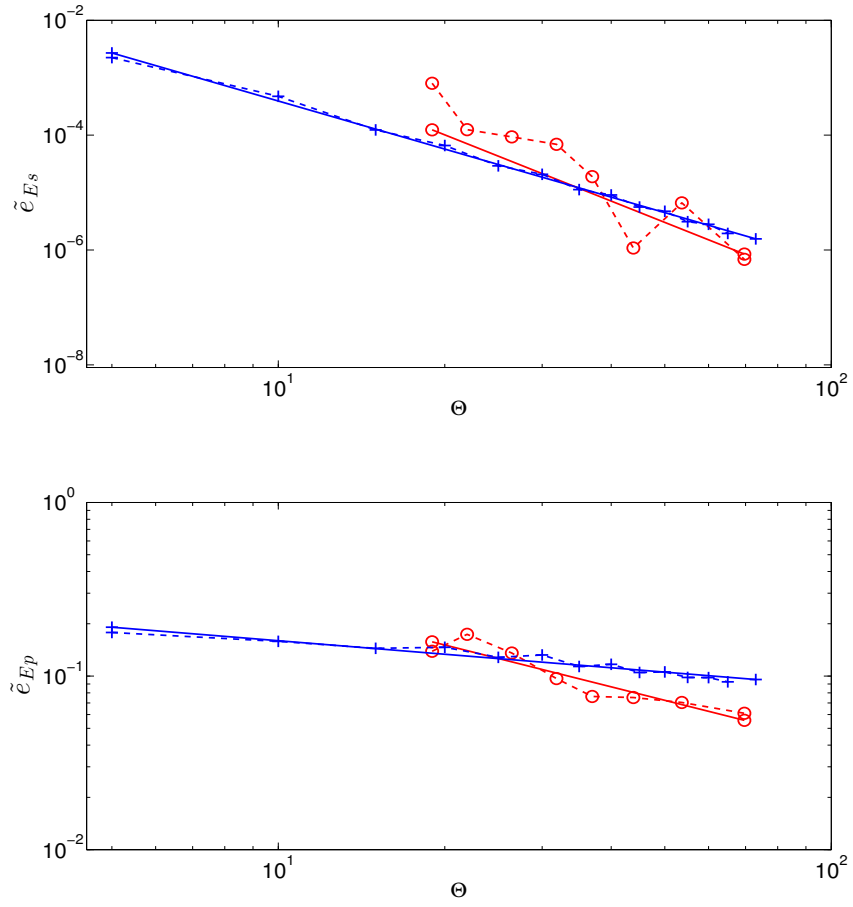


FIG. 6. Sequences of (top)  $\tilde{e}_{E_s}$  and (bottom)  $\tilde{e}_{E_p}$  versus  $\Theta$  calculated with the RCWA (data points identified by +) and MRFEM (data points identified by o) when  $\theta = 30^\circ$ . The dashed lines guide the reader's eyes. The solid lines are least-squares linear fits.

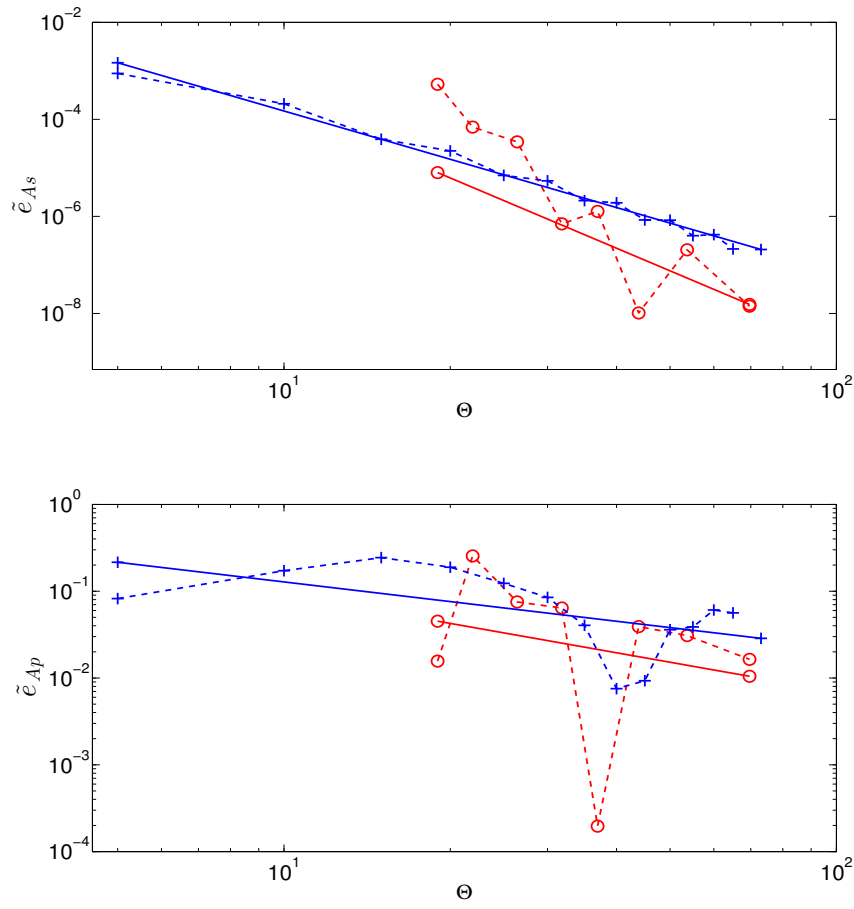


FIG. 7. Same as Fig. 6, except that (top)  $\tilde{e}_{As}$  and (bottom)  $\tilde{e}_{Ap}$  are displayed.

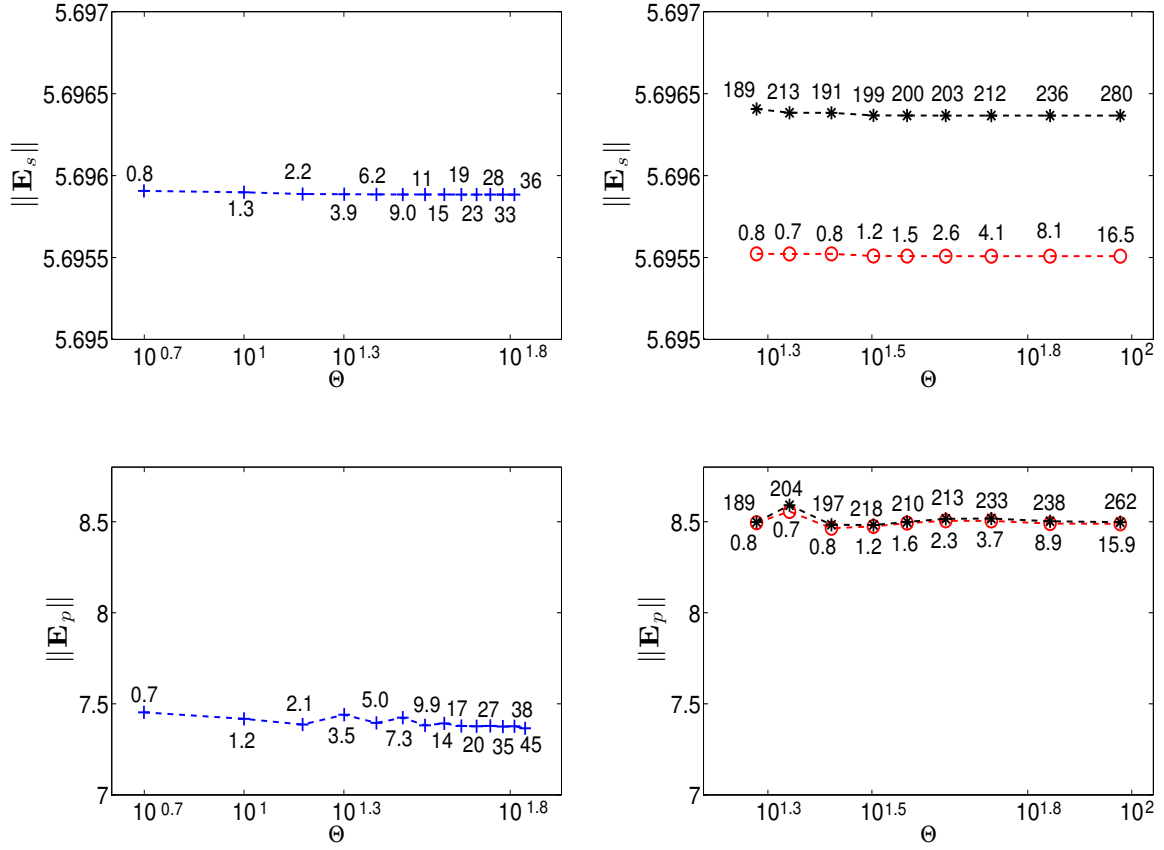


FIG. 8. Sequences of (top)  $\|\mathbf{E}_s\|$  and (bottom)  $\|\mathbf{E}_p\|$  versus  $\Theta$  calculated with the RCWA (data points identified by +), the MRFEM with  $M_t = 1$  (data points identified by o), and the MRFEM with  $M_t = 20$  (datapoints identified by \*), when  $\theta = 0^\circ$ . The numbers stated near the data points are the computational times in seconds. The dashed lines guide the reader's eyes.

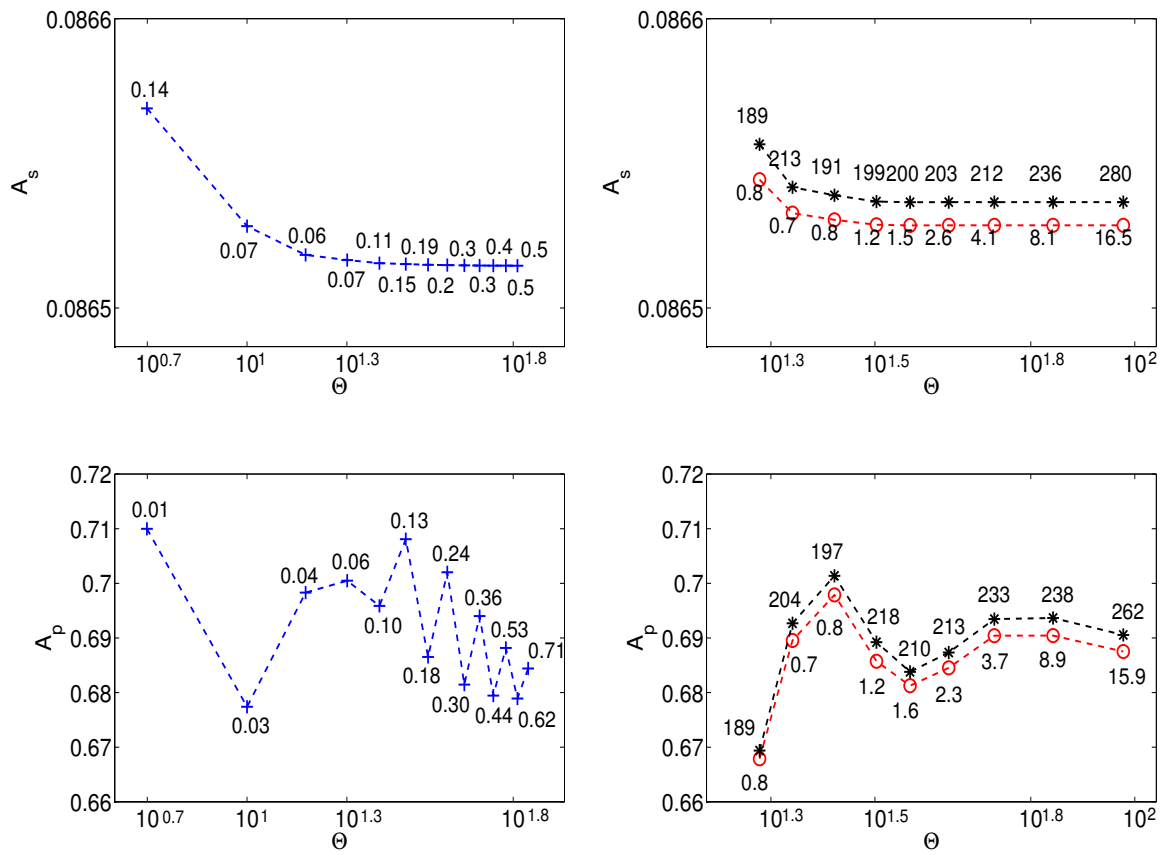


FIG. 9. Same as Fig. 8, except that (top)  $A_s$  and (bottom)  $A_p$  are displayed.

# Centro de Investigación en Ingeniería Matemática (CI<sup>2</sup>MA)

## PRE-PUBLICACIONES 2014

- 2014-05 ANA ALONSO-RODRIGUEZ, JESSIKA CAMAÑO, RODOLFO RODRÍGUEZ, ALBERTO VALLI: *Assessment of two approximation methods for the inverse problem of electroencephalography*
- 2014-06 GABRIEL N. GATICA, RICARDO RUIZ-BAIER, GIORDANO TIERRA: *A mixed finite element method for Darcy's equations with pressure dependent porosity*
- 2014-07 GABRIEL N. GATICA, GEORGE C. HSIAO, SALIM MEDDAHI, FRANCISCO J. SAYAS: *New developments on the coupling of mixed-FEM and BEM for the three-dimensional exterior Stokes problem*
- 2014-08 HERNÁN MARDONES, CARLOS M. MORA: *First-order weak balanced schemes for bilinear stochastic differential equations*
- 2014-09 RODOLFO ARAYA, ABNER POZA, FREDERIC VALENTIN: *A low-order local projection method for the incompressible Navier-Stokes equations in two and three dimensions*
- 2014-10 JULIEN CASSAIGNE, NICOLAS OLLINGER, RODRIGO TORRES: *A small minimal aperiodic reversible Turing machine*
- 2014-11 VERONICA ANAYA, GABRIEL N. GATICA, DAVID MORA, RICARDO RUIZ-BAIER: *An augmented velocity-vorticity-pressure formulation for the Brinkman problem*
- 2014-12 SEBASTIANO BOSCARINO, RAIMUND BÜRGER, PEP MULET, GIOVANNI RUSSO, LUIS M. VILLADA: *Linearly implicit IMEX Runge-Kutta methods for a class of degenerate convection-diffusion problems*
- 2014-13 FABIÁN FLORES-BAZÁN, ABDERRAHIM JOURANI, GIANDOMENICO MASTROENI: *On the convexity of the value function for a class of nonconvex variational problems: existence and optimality conditions*
- 2014-14 FABIÁN FLORES-BAZÁN, NICOLÁS HADJISAVVAS, FELIPE LARA: *Second order asymptotic analysis: basic theory*
- 2014-15 ANAHI GAJARDO, CAMILO LACALLE: *Revisiting of 2-pebble automata from a dynamical approach*
- 2014-16 MUHAMMAD FARYAD, AKHLESH LAKHTAKIA, PETER MONK, MANUEL SOLANO: *Comparison of rigorous coupled-wave approach and finite element method for photovoltaic devices with periodically corrugated metallic backreflector*

Para obtener copias de las Pre-Publicaciones, escribir o llamar a: DIRECTOR, CENTRO DE INVESTIGACIÓN EN INGENIERÍA MATEMÁTICA, UNIVERSIDAD DE CONCEPCIÓN, CASILLA 160-C, CONCEPCIÓN, CHILE, TEL.: 41-2661324, o bien, visitar la página web del centro: <http://www.ci2ma.udec.cl>



**CENTRO DE INVESTIGACIÓN EN  
INGENIERÍA MATEMÁTICA (CI<sup>2</sup>MA)  
Universidad de Concepción**



Casilla 160-C, Concepción, Chile  
Tel.: 56-41-2661324/2661554/2661316  
<http://www.ci2ma.udec.cl>



---